Elucidating large-scale atmospheric controls on Bering Strait throughflow variability using a data-constrained ocean model and its adjoint

An T. Nguyen[1*], Rebecca A. Woodgate[2], and Patrick Heimbach[1]

[1]University of Texas at Austin, Austin, TX, USA
[2]University of Washington, Seattle, WA, USA

Key Points:

- An adjoint sensitivity analysis is performed to quantify the role of atmospheric forcing on the variability of Bering Strait throughflow
- Primary driver of the variability is the wind stress over the Bering Sea and Arctic shelves, on timescales matching shelf wave propagation
- Impact of precipitation, although consistent with steric flow control, yield insignificant variability on monthly to interannual timescales

*Oden Institute for Computational Engineering and Sciences, The University of Texas at Austin, Austin, TX, USA

Corresponding author: An T. Nguyen, `atnguyen@oden.utexas.edu`

Abstract

A data-constrained coupled ocean-sea ice general circulation model and its adjoint are used to investigate mechanisms controlling the volume transport variability through the Bering Strait from 2002 to 2013. Comprehensive time-resolved sensitivity maps of the Bering Strait transport to atmospheric forcing can be accurately computed with the adjoint along the forward model trajectory to identify the spatial and temporal scales most relevant to the strait's transport variability. The model's Bering Strait transport anomaly is found to be controlled primarily by the wind stress on short time-scales of order 1 month. Spatial decomposition indicates that on monthly time-scales winds over the Bering and the combined Chukchi and East Siberian Seas are the most significant drivers. Continental shelf waves and coastally-trapped waves are suggested as the dominant mechanisms for propagating information from the far field to/from the strait. In years with transport extrema, eastward wind stress anomalies in the Arctic sector are found to be the dominant control, with correlation coefficient of 0.94. This implies that atmospheric variability over the Arctic plays a substantial role in determining the Bering Strait flow variability. The near-linear response of the transport anomaly to wind stress allows for predictive skill at interannual time-scales, thus potentially enabling skillful prediction of changes at this important Pacific-Arctic gateway, provided that accurate measurements of surface winds in the Arctic can be obtained. The novelty of this work is the use of space and time-resolved adjoint-based sensitivity maps, which enable detailed dynamical, i.e. causal attribution of the impacts of different forcings.

Plain Language Summary

An ocean circulation model, that was adjusted to match observations, is used to investigate what are the important factors controlling the oceanic flow of water through the Bering Strait. Results show that the flow through the strait is related to surface atmospheric winds over the Bering Sea Shelf (south of the strait) and the near coastal regions of the Arctic Ocean (north of the strait). In the model, knowledge of these winds over the preceding 1 month allows us to reconstruct most of the changes in the flow through the strait. A somewhat surprising result is that winds in the Arctic have a greater influence on the amount of water flowing through the Bering Strait than winds over any region of the Pacific Ocean or the Bering Sea. The connection between the winds and the flow through the strait is strong enough that interannual changes in the winds may be used to predict interannual change in the flow. This predictive skill opens up the prospect for an improved understanding of the causes and mechanisms of flow changes at this important Pacific-Arctic gateway, provided that accurate measurements of surface winds over the Arctic can be obtained.

1 Introduction

The narrow (∼85 km wide) and shallow (∼50 m deep) Bering Strait is the only oceanic connection between the Pacific and the Arctic oceans (Fig. 1a). The annual mean flow is about 0.8 Sv (1 Sv = 10^6 m^3/s), northward through the strait, with a seasonal cycle ranging from $\sim$ 0.4 Sv to 1.4 Sv, and with significant interannual variability (Woodgate et al., 2005a, 2006, 2012). The Pacific waters carried by the flow (typically fresher than most Arctic waters, and seasonally warm and cold) contribute significantly to the stratification, as well as the heat, freshwater and nutrient budgets of the Chukchi Sea and the Arctic Ocean , (*e.g.*, Woodgate et al. (2005b); Serreze et al. (2006, 2007, 2016); Walsh et al. (1997); see Woodgate et al. (2015) and Woodgate (2018) for reviews.) The Pacific Waters eventually exit the Arctic into the North Atlantic via the Fram Strait, Nares Strait, and the Canadian Arctic Archipelago, thus influencing the world ocean circulation (*e.g.*, De Boer and Nof (2004b, 2004a); Hu and Meehl (2005); Hu et al. (2012); for a review, see Wadley and Bigg (2002)). Closer to the source, within the Chukchi Sea and possibly the western Arctic Ocean, the inflow of warm Pacific waters is shown to influence sea-ice retreat (Woodgate et al., 2010; Serreze et al., 2016). This in turn affects light availability in the water column on the Chukchi Shelf, which, in combination with nutrient supply, may modulate regional in-ice (Arrigo, 2014) and under-ice (Arrigo et al., 2012) ecosystem activity.

Given the influential role of the Bering Strait throughflow, including its potential societal impacts (e.g., driving changes important for Arctic residents, and industrialization, such as resource exploitation and Arctic shipping/fishing), it is important to quantify the properties of the flow and, where possible, understand the mechanisms controlling how those properties change. Year-round in situ observations in the strait have been obtained nearly continually since 1990 (see Woodgate et al. (2015) for a review) and have indicated significant increases in volume ($\sim$ 0.6–1.1 Sv), heat and freshwater transports at least from the early 2000s to present (2018) (Woodgate et al. (2015); Woodgate (2018), Woodgate, unpublished data). To date, however, the causes for these changes remain poorly understood.

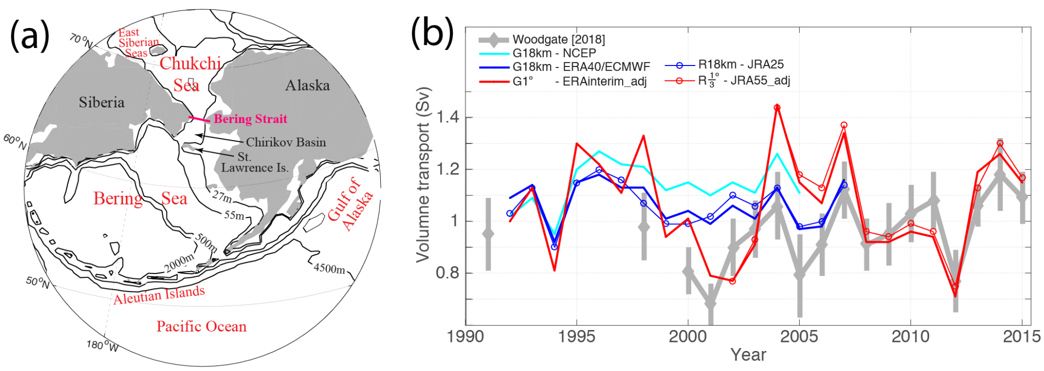

Figure 1. (a) Geographic location of the Bering Strait, showing bathymetric contours from IBCAO (Jakobsson et al., 2012). (b) Annual mean northward volume transport through Bering Strait (BE), estimated from various sources: in situ moorings observations (including a standard correction for the Alaskan Coastal Current, thick grey, with error bars, Woodgate (2018)); global (G, thick color lines) and regional (R, thin color lines with symbol) ECCO configurations using various atmospheric reanalyses and model horizontal grid resolutions (given in legend). The atmospheric reanalyses are NCEP/NCAR (Kalnay et al., 1996), ERA-40/ECMWF (Uppala et al., 2005), JRA25 (Onogi et al., 2007), ERA-Interim (Dee et al., 2011), and JRA55 (Kobayashi et al., 2015). Simulations marked with extension "adj" are from adjoint-based optimization, where the atmospheric forcing fields have been adjusted within their respective uncertainties to bring the model into agreement with satellite and in situ observations, including Bering Strait mooring data (Forget et al., 2015; Fenty et al., 2015).

Typically the flow through the Bering Strait is attributed to a large scale oceanic "pressure head" forcing (usually cited as the difference in sea surface height between the Pacific and the Arctic oceans), modified by local wind forcing within the strait (see Woodgate et al. (2005b); Woodgate (2018) for discussion). This hypothesis was first discussed in the international literature by Coachman and Aagaard (1966), a work which summarized some of the prior Russian studies in the region, and, as other authors, tacitly assumed the pressure head forcing to be quasi constant in time. While the hourly variability of the throughflow is extremely well correlated with the local wind (correlation coefficient $\sim$ 0.8), longer term variability is not well explained by variations in the local wind, leading to the suggestion that longer term change relates to variability in the pressure head drivings of the flow (Woodgate et al., 2010, 2012; Woodgate, 2018; Peralta-Ferriz & Woodgate, 2017).

The details of this pressure head forcing, however, have long remained very unclear. The origin of the pressure head has been suggested to be either steric (Stigebrand, 1984) or driven by global winds (*e.g.*, De Boer and Nof (2004b, 2004a)). More recently, using a conceptual model, Danielson et al. (2014) correlated winds, pressure, and sea surface heights north and south of the strait with the throughflow and suggested that the Bering shelf circulation is highly controlled by basin scale wind patterns, particularly the Aleutian Low in the Bering Sea/Gulf of Alaska, with additional contributions from the Beaufort and Siberian Highs and modifications from coastal shelf waves. Yet more recent work (Peralta-Ferriz & Woodgate, 2017) finds high correlations (correlation coefficient $\sim$0.6) between monthly flow variability and a specific pattern of ocean bottom pressure (OBP) data, viz a pattern dominated by low OBP in the East Siberian Sea (ESS) (assisted in winter by high OBP over the Bering Sea Shelf). Although that study excludes interannual trends, it suggests a mechanism whereby westward Arctic coastal winds invoke northward Ekman transport over the ESS, enhancing the sea-level difference between the Pacific and the Arctic and thus reducing sea level in the ESS and drawing flow northward through the strait. A distinction to prior work is that Peralta-Ferriz and Woodgate (2017) suggests the monthly variability of the flow is primarily driven by Arctic processes, not Bering Sea processes.

All of the above mentioned studies, however, are based on either simple theoretical or statistical models. The complexity of the system suggests that progress on understanding the large-scale mechanism controlling the throughflow may be made by drawing on the much more complete numerical simulations of coupled sea ice-ocean general circulation models. In particular, we will utilize the non-linear inversion ("adjoint") framework established within the global ECCO (Estimating the Circulation and Climate of the Ocean) version 4 coupled ice-ocean configuration (Forget et al., 2015; Heimbach et al., 2019), which is based on the Massachusetts Institute of Technology general circulation model (MITgcm) and its adjoint.

Unlike a perturbation simulation that quantifies the impact of the change of *one input* on *all outputs* (directional derivative information), the adjoint model simulation quantifies the sensitivity of *one output* to *all inputs* (gradient information). The adjoint model provides a dynamical link between the changed output quantity of interest (QoI), such as the transport through the Bering Strait, and the inputs by using the the formal transpose of the linearized equations of motion to propagate the change of one output back in time to assess its sensitivity to changes in any input. With this framework, the flow of information (e.g., sensitivity of the transport to the forcings) can be tracked from Bering Strait back to its sources in space and time (Heimbach et al., 2010; Fukumori et al., 2015; Pillar et al., 2016). Compared to purely statistical approaches (e.g., lag correlations or empirical orthogonal function decomposition), this adjoint approach provides a robust causal description. It elucidates mechanisms driving the variability and allows for the assessment of time-lagged influences. For this study, we considered several adjoint model configurations ranging from global 1° to regional 1/3° resolution prior to choosing the ECCOv4 configuration. The narrowness and shallowness of the Bering Strait suggest that a regional high resolution model configuration would be more appropriate than a global and coarser resolution one. In practice, however, we have consistently observed that, in the global MITgcm simulations (i.e., those which do not prescribe a set flow through the Bering Strait), a variety of model resolutions and wind forcing all produce similar, roughly 1 to 1.1 Sv annual mean northward flow through the Bering Strait (Fig. 1). While at smaller grid spacings the local circulation in the Bering and Chukchi Seas becomes more detailed, we do not, however, see any systematic change in the total volume of the throughflow with higher resolution. In addition, when a regional configuration (R) takes lateral boundary conditions from a global configuration, the Bering Strait (BE) transport is largely determined by the imposed lateral boundary conditions, irrespective of regional surface atmospheric forcing. This is evidenced by noting the similarity between the R1/3° run with JRA55 forcing (red line with symbol), which takes lateral boundary conditions from the global G1° run with ERA-Interim (red line) or R18km (blue line with symbol), and the global run G18km with ERA40/ECMWF (blue line). All these reasons, in addition to computational efficiency, point to a global configuration at 1° as a sufficient choice for investigating large-scale controlling mechanisms for the BE transport in our study.

Fig. 1 shows estimates of Bering Strait volume transport based on observations and various ECCO model solutions. In general, the ensemble of model simulations, which use a variety of atmospheric forcings, encompass the range of the observed transports, although there are differences in year-to-year variations and in long term trends, which show increasing flow in the observational data Woodgate (2018). For example, comparison between simulated and observed BE transport trends show more consistency for the period 2008–2015 (simulated: 0.04 Sv/yr , observed: 0.03 Sv/yr, correlation coefficient: 0.9) than for the period 2004–2012 (simulated: -0.07 Sv/yr, observed: 0.01 Sv/yr, correlation coefficient: 0.2). The latter discrepancy between simulations and data is largely due to the anomalously high transport in 2004 and low transport in 2011, seen more extremely in the models than in the data. However, we emphasize that the focus of this study is not on attempting to strictly reproduce the observed Bering Strait transport time-series over the decades. Instead, our goal is to deconstruct the time-series of the state estimate to identify the dominant regions, physical processes, and time-scales that control the flow in the underlying dynamical model. Such information may then be used to understand possible causes of real world change and identify reasons for discrepancies between the models and the observations.

This paper is organized as follows. Section 2 describes the model configurations, the adjoint sensitivity experiments by which the sensitivity of the Bering Strait transport to various input atmospheric forcings are computed, and the procedure by which we then use these sensitivities to reconstruct the transport anomalies. Section 3 investigates the spatial and temporal patterns of the adjoint sensitivities and quantifies the contributions of atmospheric forcings at various time-scales (interannual, seasonal, and sub-monthly) to the Bering Strait transport. Section 4 discusses the regions found to be most influential on the variability of the throughflow and the underlying physical mechanisms. In addition, it considers the role of precipitation as the steric driving mechanism of the Bering Strait transport variability. The transport extrema between 2004–2007 seen in the model are also discussed. Section 5 summarizes the key findings.

2 Methodology

2.1 Model description

The ECCO version4 release 2 (ECCO-v4) global ocean-sea ice state estimate at nominally 1 degree horizontal resolution (Forget et al., 2015; Fukumori et al., 2018) is the primary modeling tool in this study. The term “state estimate” here refers to the result of a data assimilation procedure by which a general circulation model is fit, in a least-squares sense, to a wide range of observations . Unlike in “reanalyses”, the assimilation procedure is such that the underlying conservation laws as expressed by the governing equations for momentum and tracers are strictly enforced, thus enabling accurate analyses of budgets and causal mechanisms (Stammer et al., 2016; Wunsch & Heimbach, 2007, 2013).

We summarize here only the salient features of the configuration that are relevant for our investigation. A more thorough description of this ECCO state estimate can be found in Forget et al. (2015). The configuration used in this study utilizes the full adjoint capability developed within the ECCO consortium (Wunsch & Heimbach, 2007, 2013; Heimbach et al., 2019). Grid spacing at the Bering Strait is ∼48 km in the horizontal and 10 m in the vertical. Although this gives only two grid points across the Bering Strait, as discussed earlier and shown in Fig. 1b, the total transport is at the strait are very similar to that in the high resolution models. The observational constraints used for the assimilation in ECCO-v4 include as many ocean and sea ice observations as available and practical, including satellite SSH, SST, Argo, ITP, and moorings at important Arctic and Nordic Seas gateways (see Forget et al. (2015) for a complete list). Note that Bering Strait mooring data have been included as a constraint.

The coupled ocean-sea ice adjoint model has been generated by means of algorithmic differentiation (AD; (Heimbach et al., 2010; Fenty & Heimbach, 2013)). Model-data misfits are reduced systematically through gradient-based iterative minimization of a least-squares misfit function (adjoint or Lagrange Multiplier method) by adjusting model parameters and input fields (together termed "control variables"), which carry sizable uncertainties (Forget et al., 2015; Stammer, 2005; Fenty & Heimbach, 2013). For the current study, the control variable space Ω is comprised of the seven atmospheric forcing fields: 10-m east- and north-ward wind stresses, precipitation, downward short- and long-wave radiation, surface specific humidity, and 10m air temperature. Uncertainties for these control variables are described in Fenty and Heimbach (2013); Chaudhuri et al. (2013, 2014). The ECMWF ERA-Interim atmospheric reanalysis (Dee et al., 2011) serves as first-guess surface atmospheric state that is subject to adjustment during the assimilation process. The model is also forced with monthly-mean estuarine runoff, which are based on the Regional, Electronic, Hydrographic Data Network for the Arctic Region (R-ArcticNET) dataset (Lammers & Shiklomanov, 2001; Shiklomanov et al., 2006). This runoff is not part of the control space and therefore not adjusted during the assimilation procedure.

2.2 Adjoint sensitivity and reconstruction

The forward and adjoint models can be used to assess how variability in the surface atmospheric forcings influence the flow through the Bering Strait by the following procedure. The model is first integrated forward in time from 2002–2013. The mean Bering Strait volume transport at a time t, $J(t)$ over a period T starting from any given time $t - T/2$ is defined as:

$$J(t) \equiv \frac{1}{T}\int_{t-T/2}^{t+T/2}\int_{A} \mathbf{u}(t')\cdot\hat{\mathbf{n}}\; dA\; dt' \tag{1}$$

where $\mathbf{u}$ is the time-varying 2-D horizontal velocity field on a vertical section across the strait, and A is the cross-sectional area of the strait whose normal component is $\hat{\mathbf{n}}$. The anomaly δJ is defined as $J(t)$ minus $\overline{J_{2002-2013}}$, which is the time-mean of our integration period of 2002–2013:

$$\delta J(t) \equiv J(t) - \overline{J_{2002-2013}} \tag{2}$$

In the adjoint mode, we seek sensitivities $\partial J/\partial\Omega$ of J to all control variables that are part of the control vector Ω. In the following we will interchangeably refer to these $\partial J/\partial\Omega$ as "sensitivities", "gradients", "influences", and "partial derivatives". The gradients can be efficiently computed for a very high-dimensional control space via the adjoint method (Wunsch & Heimbach, 2007, 2013), i.e. one adjoint integration yields all partial derivatives $\partial J/\partial\Omega_k$ simultaneously for each of the individual surface atmospheric forcing variables Ω_k. The gradients consist of two-dimensional surface fields (in x_1, x_2) and these derivatives are updated at regular (e.g., bi-weekly) intervals (linearly interpolated in between) along the model temporal trajectory. Their spatial and temporal patterns can be used to reconstruct (in the sense of a Taylor series expansion) the forward time-series of the throughflow ***anomalies*** $\widetilde{\delta J}(t)$ as follows (Fukumori et al., 2015; Pillar et al., 2016),

$$\widetilde{\delta J}(t) = \sum_k \widetilde{\delta J}_k(t) = \sum_k \int_{t_0}^{t} \int_{x_1} \int_{x_2} \frac{\partial J}{\partial \Omega_k}(x_1, x_2, \alpha - t)\, \delta\Omega_k(x_1, x_2, \alpha) dx_1 dx_2 d\alpha \qquad (3)$$

where $\widetilde{\delta J}(t)$ is the reconstructed transport anomaly, with the $\sim$ symbol added to distinguish it from the anomaly obtained from the forward run δJ_{fw}. t_0 is the time when the model integration starts which is 01/Jan/2002, α is a time prior to the current time t with possible values thus ranging from t_0 to t, $(\alpha - t)$ is the time-lag, $\delta\Omega_k$ the atmospheric forcing anomalies associated with the forcing field k, and $\partial J/\partial\Omega_k(x_1, x_2, \alpha{-}t)$ gives the influence on δJ of variable $\delta\Omega_k$ at lag time $\alpha{-}t$ and spatial location $[x_1, x_2]$.

Eqn. (3) indicates that the anomaly $\widetilde{\delta J}(t)$ at any time t is a convolution of the time-lagged $(\alpha{-}t)$ gradient $\partial J/\partial\Omega$ with the forcing anomaly $\delta\Omega$ at time α. In simpler language the equation states that the reconstructed anomaly $\widetilde{\delta J}(t)$ is computed from the sum of point-wise influences (in space and time) integrated over the time α, which ranges from t_0 to the time t of consideration. This implies that contributions to the transport anomaly $\delta J(t)$ at any time t will depend on how sensitive $\delta J(t)$ is to each forcing anomaly $\delta\Omega_k$ at various time-lags corresponding to prior days, months or years, and the spatial distribution of the sensitivity up- and down-stream of the strait. Note that the time-lag $(\alpha{-}t)$ only takes on negative values, indicating that a past event has influence on a future δJ. If the system is sufficiently linear, the reconstructed $\widetilde{\delta J}(t)$ will be close to the full $\delta J_{fw}(t)$ obtained with the full nonlinear forward model.

Although in theory, $\partial J/\partial\Omega$ may vary with the time when J is defined, a reasonable approximation is to assume that if there is a dominant linear mechanism linking the drivers $\delta\Omega$ with δJ, then $\partial J/\partial\Omega$ should be, to first order, independent of the time when J is defined. Tests (see Supplemental Material) show this to be the case, and thus in what follows, we use $\partial J/\partial\Omega$ that correspond to a J defined as the monthly mean Sept 2013 transports. This choice of $J_{Sep/2013}$ is based on the consideration that the September transports lie between the seasonal transport extrema (Woodgate et al., 2005a) with maximum δJ during the summer months and minimum δJ during the winter months. With J defined as $J_{Sep/2013}$, we compute time-lagged gradients $\partial J/\partial\Omega$ at discrete, monthly intervals.

3 Results

3.1 Adjoint sensitivity maps

Monthly average adjoint sensitivities were computed for all seven atmospheric control variables at different monthly-averaged lag times. The largest influence found was related to surface wind stress. Sensitivities with respect to meridional (N) and zonal (E) wind stress $\frac{\partial J}{\partial \tau_N}$ and $\frac{\partial J}{\partial \tau_E}$ are highest within lag of $|\alpha{-}t| = 1$ month (the shortest calculated lag), and both wind stress components contribute significantly to $\delta J(t)$ (Fig. 2).

The largest sensitivities are found (not surprisingly given prior results) in the strait itself, with $\frac{\partial J}{\partial \tau_N}$ being approximately (in magnitude) two times larger than $\frac{\partial J}{\partial \tau_E}$. This is consistent with the observational result showing that the northward flow through the strait is best correlated with the wind at heading 330deg (Woodgate et al., 2005b). Away from the strait, the largest sensitivities are found over the shallow shelves south and north of the strait, especially the Bering Sea Shelf above 500 m (for northward wind stress), the Gulf of Alaska, the Chukchi Sea, and the East Siberian Sea shelf break. Within these regions, over the northern Bering Sea Shelf between 0–150 km south of the strait, τ_N has the strongest impact on the strait transport at up to 1-month lag, with positive wind

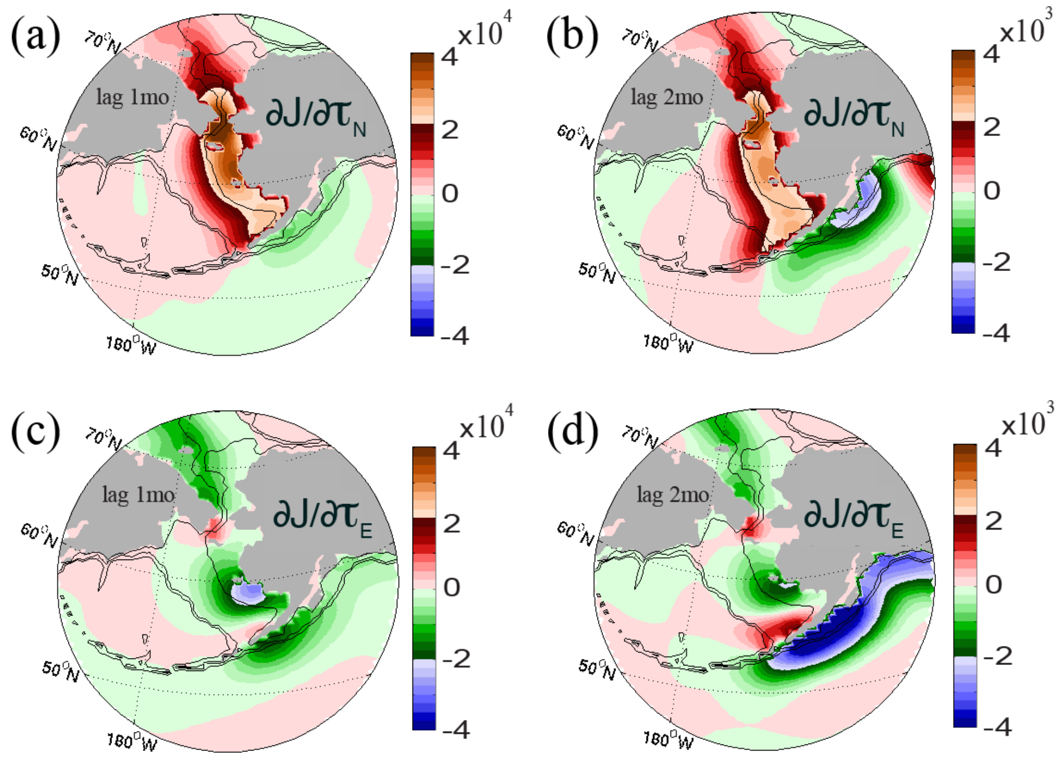

Figure 2. Sensitivity of Bering Strait volume transport anomalies to increments in (a–b) northward wind stress $\frac{\partial J}{\partial \tau_N}$ and (c–d) eastward wind stress $\frac{\partial J}{\partial \tau_E}$ in units of $(m^3/s)/(N/m^2)$ at (a,c) 1-month and (b,d) 2-month lags (see Section 2.2 and eqn (3) for the definition of lag.) A positive gradient here implies that a positive increment $\delta\tau_{E,N}$ will result in a positive increase in the $\widetilde{\delta J}$ with magnitude as indicated in the color scales and units. The highest sensitivity of order $\sim\ 10^4$ (m^3/s)/(N/m^2) is found within a time-lag of 1-month and is highly localized to the Bering Strait and shallow Bering and Chukchi Sea shelves. Bathymetric contours are the same as shown in Fig 1a.

change over the Bering Sea Shelf resulting in positive increase in Bering Strait transport (see the range in the color-scale in Fig. 2a). The combination of positive $\partial J/\partial\tau_N$ and negative $\partial J/\partial\tau_E$ parallel to and between the Alaskan coast and the 500 m isobath in the Bering Sea implies that northwestward wind stress here promotes positive δJ, likely via a mechanism of onshelf transport.

Away from the strait, there exist several regions with significant influences as well. In particular, southeast of the Aleutian islands, negative $\partial J/\partial\tau_N$ and $\partial J/\partial\tau_E$ along the Alaskan coast and the Aleutian Islands suggest that southwestward wind stress in this region promotes the strengthening of the Alaska Coastal Current (Weingartner et al., 2005), leading to enhanced northward flow through the Aleutian Islands onto the Bering Shelf and also increasing δJ at the Bering Strait at lags of 1–2 months. These results are consistent with statistical wind-to-transport correlations of Danielson et al. (2014).

Inside the Arctic, positive $\partial J/\partial\tau_N$ and negative $\partial J/\partial\tau_E$ indicate northwestward wind stress anomalies in the Chukchi and East Siberian Seas promote δJ increases likely by the mechanism suggested by Peralta-Ferriz and Woodgate (2017), who find significant correlations between westward winds along the East Siberian Sea shelf break and the flow through the Bering Strait, especially with the component of the flow not associated with the local wind (i.e., the pressure head term, Woodgate (2018)). Peralta-Ferriz and Woodgate (2017) propose a mechanism by which these westward winds in the Arctic draw waters off the East Siberian Sea shelf via Ekman processes, lowering sea level in the East Siberian Sea, and drawing waters north through the Bering Strait (as per the theory of flow through a rotating channel, see e.g., Toulany and Garrett (1984)). These regions (both south and north of the strait) are suggested areas of formation of shelf waves that may contribute to driving Bering Strait transport anomalies (Danielson et al., 2014). Section 4 discusses in more detail shelf waves as a mechanism for propagation of sensitivities to the Bering Strait.

At a 2-month time lag, sensitivities drop approximately one order of magnitude, and are spread further north and south of the strait (Fig. 2b,d). All patterns and signs of $\partial J/\partial\tau_{E,N}$ remain consistent with those within the 1-month lag. Additional features include those further south along the western Canadian coast, where an increase in northwestward wind stress promotes a positive δJ at the strait two months later. Within the Arctic, southwestward wind stress anomalies in the Kara Sea and much further away in the eastern Nordic Sea (both not shown) also appear to have some influence on the BE throughflow, although the magnitudes of sensitivity is significantly reduced such that their overall contribution to δJ is negligible (see further discussion in Section 3.4).

After two months, the sensitivities decrease by another factor of 5–10, such that their contribution to the transports is insignificant (not shown).

3.2 Reconstruction of transport anomaly time series

The sensitivities seen in Fig. 2 suggest that wind stress is the dominant driver of the throughflow at Bering Strait in the model. To confirm this, we reconstruct the transport anomaly time series by summing the contributions from $\partial J/\partial\Omega$ globally, following eqn. (3). Fig. 3 shows δJ_{fwd} obtained from the model forward run (black) and $\widetilde{\delta J}$ from the reconstruction via eqn. (3) (red, blue). Two reconstructions were made, one using only contributions from the northward and eastward wind stress anomalies (blue in Fig. 3) for the purpose of isolating the role of winds, and one using contributions from all seven atmospheric forcing fields (red) for the purpose of assessing the role of the non-wind stress terms. Also shown are the correlation coefficient ρ and percentage of explained variance (PEV) between the forward and reconstructed time series.

The reconstructed time series $\widetilde{\delta J}_{all}$ (red) correlates strongly ($\rho > 0.94$) with the model's forward time series δJ_{fwd} (black) at all time lags (Fig. 3c–f), with slopes in the scatter plots of $\widetilde{\delta J}_{all}$ versus δJ_{fwd} ranging between 0.96 and 1.01. This suggests that the reconstruction captures nearly the full dynamics of the strait transport anomalies in the model. Note that the reconstruction using only the 1 month lag contribution still captures $\sim$90% of the variability and 96% of the magnitude (slope on scatter plot). Additionally, the wind stress components are the dominant contributors to the transport anomalies at monthly to multi-year time-scales, with all other atmospheric forcing terms contributing only $\sim$1–2% (compare the slope of "all" versus $\tau_{E,N}$ in Fig. 3c-f).

A noticeable degradation of ρ and PEV when including contributions from longer time lags can be seen when all forcing terms are included (Fig. 3b). A breakdown of contributions from individual forcing terms shows that the terms associated with heat content (e.g., air temperature, downward long and short waves) contributed approximately equally to the degradation (not shown). We speculate that these terms (e.g., downward long- and short-wave radiation and air temperature) may have an accumulated non-linear effect on the water column with time that the adjoint sensitivities cannot fully capture. As a result, errors in $\widetilde{\delta J}$ are aggregated with increasing cumulative lags the further back in time the reconstruction is carried out. This degradation in the reconstruction due to contributions from buoyancy terms has also been observed in previous adjoint-based reconstructions (see Pillar et al. (2016); Smith and Heimbach (2018), but a full investiga-

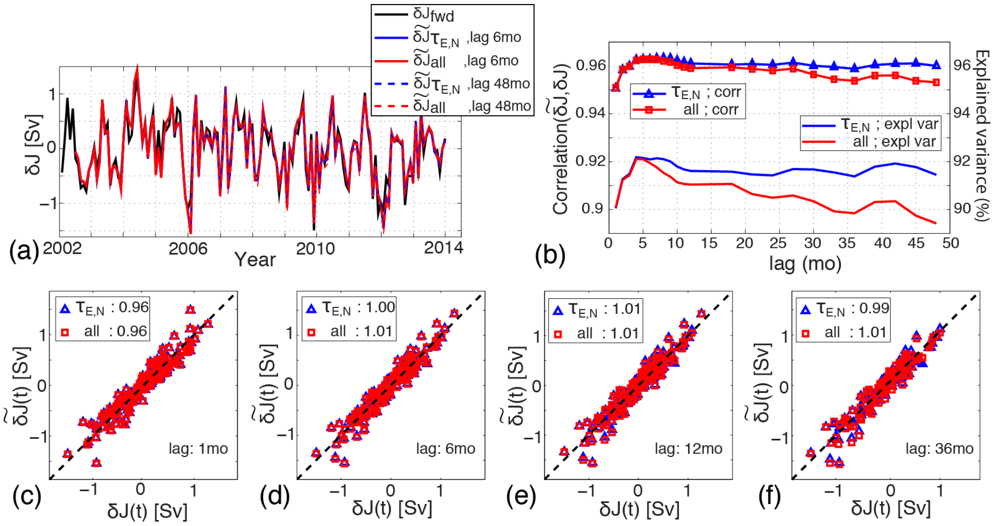

Figure 3. (a) The time series of $\widetilde{\delta J}(t)$ reconstructed using anomalies of either only wind stress (blue) or all seven atmospheric components of Ω (red), to be compared with the forward time series $\delta J_{fwd}(t)$ in black. (b) Correlation coefficient ρ between $\widetilde{\delta J}$ (the reconstructed transport anomalies) and δJ_{fwd} (the transport anomalies from the forward model; lines with symbols), along with percentage of explained variance (PEV, line without symbols, using y-axis to the right) for reconstructions which are cumulatively summed over the range of lags indicated in the abscissa. See Section 3.3 for discussion on the degradation of ρ and PEV when all atmospheric forcing terms are used in the reconstruction. (c–f) Scatter plots of the the forward δJ_{fwd} with full model dynamics versus the reconstructed time series $\widetilde{\delta J}$ for lags of up to (c) 1 month , (d) 6 months, (e) 12 months, and (f) 36 months. Numbers in the legend indicate the slope of the fitted line, with the one-to-one line shown in dashed black for reference.

tion of whether the degradation is due to inaccuracies in the linearized adjoint model or missing physics in the forward model is beyond the scope of this current study. Excluding the contributions from air temperature and downward radiation, the correlation between the $\widetilde{\delta J}$ reconstructed using wind stress and δJ_{fwd} remain steady when longer time lags are considered, suggesting that there is a close correspondence between the wind stress and the BE transport anomalies, and that the effect of winds has a short time history (Fig. 3f). Finally, adding the contribution from precipitation to $\widetilde{\delta J}$ (not shown) did not change the correlation significantly.

3.3 Decomposing $\widetilde{\delta J}(t)$ into temporal components

To examine short to long time-scale contributions, the time series of monthly transport anomaly from both the forward model δJ_{fwd} and the adjoint-based reconstruction $\widetilde{\delta J}(t)$ can also be decomposed into its monthly (sub-seasonally), seasonally (12-month climatology), and multi-year components (Fig. 4). We calculate this discretely, rather than as a spectral decomposition as our time series is comparatively short. For any time series of anomalies, the decomposition is done as follows. The 2002–2013 annual mean time series (12 annual means), denoted by subscript "y", is obtained by computing the average of the anomaly for each calendar year. The monthly climatology time series (12 monthly means), denoted by subscript "c", is computed by subtracting from each monthly value the annual average for that year, and then averaging over each month for the entirety of the record. Finally, the "residual", denoted by subscript "res", is computed by

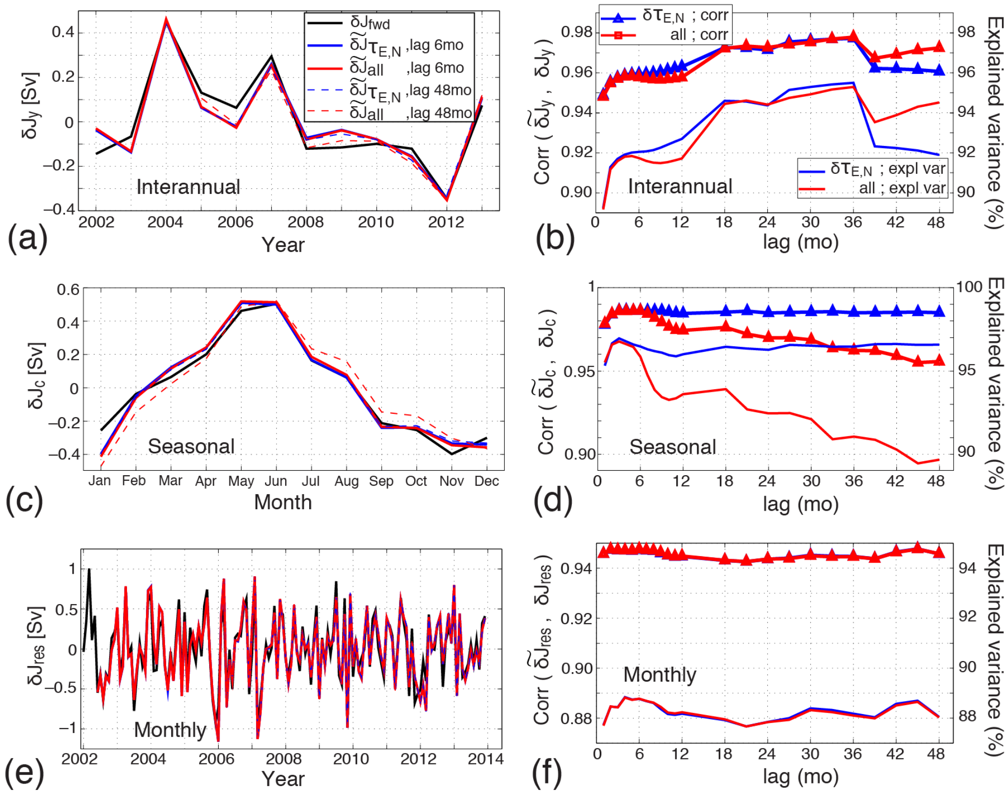

Figure 4. Decomposition of the forward model $\delta J_{fwd}(t)$ and reconstructed $\widetilde{\delta J}(t)$ into their annual mean (a), 12-mo climatology (or seasonal, c), and monthly (or high-frequency, e). Left panels (a,c,e) show the time series of each component, while right panels (b,d,f) show correlation ρ and percentage of explained variance (PEV) between the reconstructed $\widetilde{\delta J}$ and the model forward δJ_{fwd} time series for annual (b), seasonal (d) and monthly (f). See text for discussion on the degradation of ρ and PEV when all atmospheric contribution terms are included in the reconstruction of the climatological time series in (d).

subtracting from each monthly anomaly both the annual mean and the seasonal climatology for that month. The decomposition described above operates strictly on the transport anomaly time-series δJ_{fwd} or $\widetilde{\delta J}$. Note that $\widetilde{\delta J}$ is obtained from eqn. (3) using the total (i.e., non-decomposed) forcing anomalies $\delta\Omega$.

Given the dominance of wind stress forcing on δJ at short lags, as discussed in Section 3.2, we explore a second approach for the temporal decomposition that would allow us to relate directly the temporally decomposed forcings $\delta\Omega_{[y,c,res]}$ to the decomposed $\widetilde{\delta J}_{[y,c,res]}$ as follows:

$$\widetilde{\delta J}_{[y,c,res]}(t) \quad \approx \quad \int_{t_0}^{t}\int_{x_1}\int_{x_2} \frac{\partial J}{\partial \Omega_k}(x_1, x_2, \alpha - t)\ \delta\Omega_{[y,c,res],k}(x_1, x_2, \alpha)\ dx_1\ dx_2\ d\alpha \quad (4)$$

A comparison of these two approaches (i.e., a decomposition obtained from the full reconstructed $\widetilde{\delta J}$ and that obtained from approximation following eqn. (4)) can be found in the Supplemental Material. It shows that both methods yield approximately the same results. The important advantage of performing the reconstruction following the approximate method of eqn. (4) is that it is then straightforward to calculate, for example, the interannual transport anomalies $\widetilde{\delta J}_y$ from the interannual forcing anomalies ($\delta\Omega_c$) of any forcing reanalysis. Thus, all reconstructed decompositions shown in the following were obtained using eqn. (4).

Results of the reconstructed $\widetilde{\delta J}_{[y,c,res]}$ as well as comparisons of these time-filtered components to their counterparts from the forward model are shown in Fig. 4. The reconstructed time series based on annual-means, $\widetilde{\delta J}_y$ (Fig. 4a-b), captures well the model decadal trend seen in $\delta J_{fwd,y}$. It has an apparent maximum ρ and PEV when summing in time up to a lag of 36-months, but note that the change in correlation and PEV is very small (0.01 and 1%). There appears to be a small annual cycle (at every incremental 12-month lag) in both ρ and PEV, with a noticeable drop-off after 36-month (Fig. 4b). One possible cause might be that 36-months is the time-scale where linearity assumption holds and that beyond 36-months this assumption begins to break down. Note however that overall the correlation and PEV still remain very high ($\rho > 95\%$ and $PEV > 92\%$).

There is a very small difference of 1–2% between using only wind stress and using all atmospheric forcing variables for the reconstruction, implying that to first order winds are again the controlling factor, even at the multi-year time-scale, in setting the annual mean anomalies (above the long-term mean flow of ∼1 Sv). Note that for short lags the local winds dominate, but for longer lags the net effect of winds is spread out over a much larger (basin-scale) region and we will return to this in Section 3.4.

The reconstructed time series based on monthly climatological values, $\widetilde{\delta J}_c$ (Fig. 4c-d), exhibits a pronounced degradation of ρ and PEV when using all atmospheric variables (red line) after ∼6 month lag. An inspection of the reconstructed seasonal cycle of the transport anomalies (Fig. 4c) shows that as more lags are used for the reconstruction, there is a noticeable shift in timing in the entire seasonal cycle, e.g., later increase, later maximum, later decrease. As discussed in the previous section, we speculate that this degradation is due to non-linear effects of longwave and shortwave absorption in the ocean such that beyond ∼5 months the linearity assumption breaks down (Smith & Heimbach, 2018). What remains robust is that the sensitivity patterns from the first two months (Fig. 2) capture $> 98\%$ of the correlation and $\sim 97\%$ of PEV. Even after a 48 month lag, with the degradation, the PEV is still $\leq$90%. Overall, the reconstruction using only winds yields the highest correlation and PEV.

The remaining BE transport residual at sub-seasonal (monthly) time-scale, δJ_{res}, is still well reconstructed (88% of PEV) by the local wind within four months prior, with minimal improvement ($\sim 1\%$) after the first month lag (Fig. 4f).

Overall, the time-filtered reconstructions reveal that adjoint sensitivity $\partial J/\partial\Omega$ for wind stress captures 95–98% of the variability of the full time series of the BE transport anomaly at monthly to multi-year time-scales (Fig 4b,d,f). The degradation in correlation between $\widetilde{\delta J}$ and δJ_{fwd} (Fig. 3b) is largely due to degradation in the reconstructed seasonal cycle (Fig 4d). Even with the degradation, the correlation is still high, with ∼90% of the variance captured at the seasonal time-scale. As the difference in the reconstruction using all forcings and using only wind stresses is small, for the remainder of the analyses we will focus on reconstructions using only wind stress.

3.4 Decomposing $\widetilde{\delta J}(t)$ in space

Up to now, the reconstruction of $\widetilde{\delta J}$ has been performed by integrating the effect of winds over the entire globe (see eqn. 3). However, as discussed in Section 3.1, regions near the strait and further up- or down-stream can contribute coherently or non-coherently at different time lags. Fig. 5a shows a breakdown of contributions for the three most important regions, which are chosen heuristically to include what our analysis shows are the major areas of influence: (1) the Bering Sea Shelf (BeS), situated south of the strait

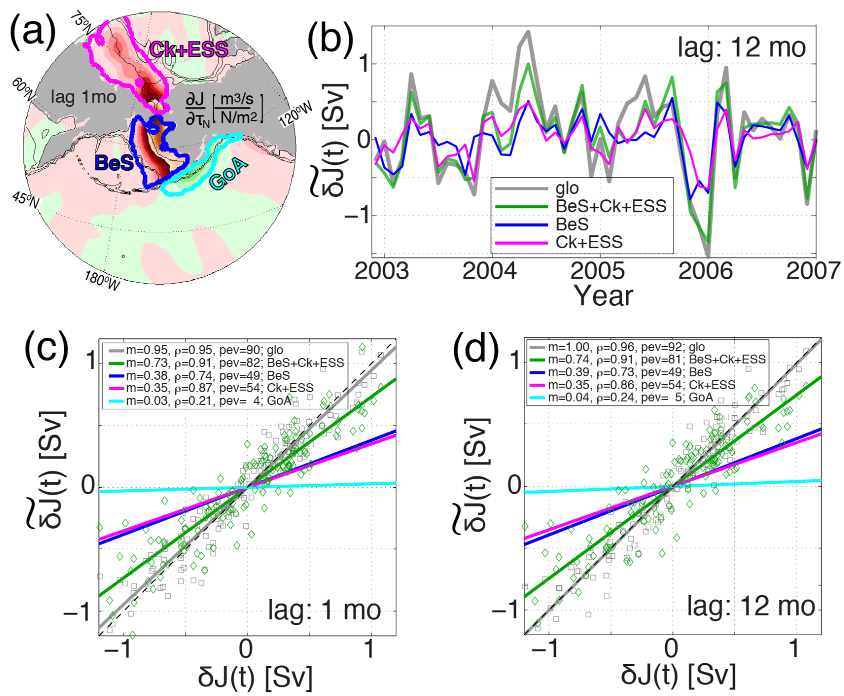

Figure 5. (a) Three regions that contribute the most to the BE transport anomalies at 1 month time lag: the Bering Sea Shelf (BeS), Gulf of Alaska (GoA), and the Chukchi and East Siberian Seas (Ck+ESS). (b) Reconstruction, using winds only, as a function of region of influence, including some combinations of regions (colors as per key) and the global sum (glo, grey line) for comparison. Scatter plot of the reconstructed $\widetilde{\delta J}$ and forward δJ_{fwd} summed to lags of (c) 1-month and (d) 12-months. Legends in (c–d) show the fitted slope (m), correlation (ρ), and percentage of explained variance (PEV).

with dominantly positive sensitivity to northward wind stress; (2) the Gulf of Alaska (GoA), situated further south of the strait with dominantly negative sensitivity to northward wind stress; and (3) the Chukchi and East Siberian Seas (Ck+ESS) situated north of the strait with positive sensitivity to northward wind stress.

The convolution restricted to over these individual regions (Fig 5b) can be compared with that from the global convolution (blue curve in Fig. 3 and Fig. 4). Only a limited period (2003–2007) of the full time series (2002–2013) is presented here to simplify the visualization of the regional contribution in individual years. With a few exceptions, regions BeS and Ck+ESS contribute approximately equally in sign and magnitude to the total month-to-month variation (each ∼40%). Region GoA contributes very little (∼4%) to the total, and is therefore omitted from Fig. 5b for clarity. The dominance of the Bering Sea Shelf and Chukchi/ESS regions can be seen clearly in the scatter plots (Fig. 5c-d) for lags of up to 12-months. Note that summing contributions up to 12-months lag does not significantly improve the reconstruction (i.e., compare BeS plus Ck+ESS 1-month lag correlation of 0.91 with BeS plus Ck+ESS 12-month lag correlation of 0.91).

Next, a more comprehensive spatial partition of the reconstruction is performed to investigate the role of local versus far field influences in modifying the seasonal and interannual variability. Seven regions were identified based on the magnitude of the adjoint sensitivity in both components of wind stress (Fig. 6). Results show that all the

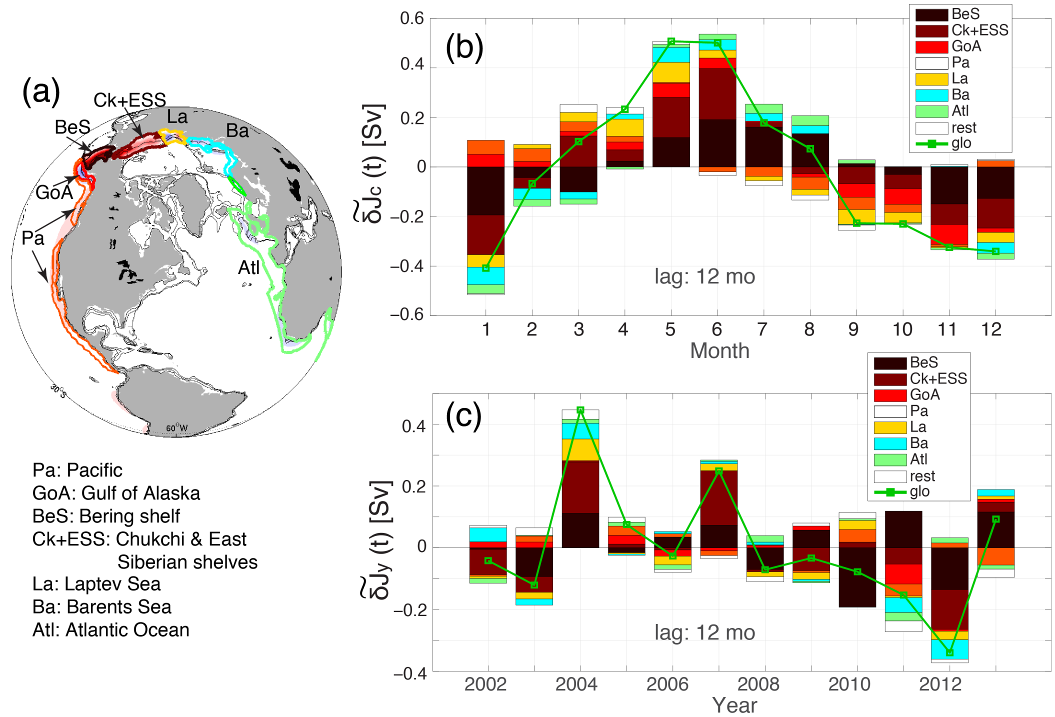

Figure 6. (a) Partition of regions of influence based on ocean regions and along important continental shelves. Reconstructions, using only $\delta\tau_{[N,E]}$ of (b) $\widetilde{\delta J_c}$ and (c) $\widetilde{\delta J_y}$ as a function of regional contributions. In (b-c), "rest" refers to the rest of the ocean excluding those regions highlighted in (a), and "glo" is the global sum. Panel (a) also links region abbreviations to their geographical location.

regions with significant influence are either over shallow high latitude shelves or along the coastlines, and all are upstream of the Bering Strait in a Kelvin wave sense. The rest of the ocean interior, labeled "rest", generally has a smaller contribution than any of the seven identified regions. A hypothesis of the factors that determine these regions will be presented in section 4.

In the reconstruction of the seasonal cycle (Fig. 6b), while the Bering and the combined Chukchi and ESS still give the largest contributions (each ∼35%), it is interesting to note the significant contributions (∼ 30%) of regions very far downstream such as the Laptev Sea (La), the Barents Sea (Ba), and the eastern North Atlantic (Atl).

In the reconstruction of the interannual time-series (Fig. 6c), the most noticeable pattern is the frequently competing contributions (e.g., contributions of opposite sign to the total $\widetilde{\delta J_y}$) between the Pacific (Pa) plus Gulf of Alaska (GoA) and the BeS plus Ck+ESS regions, although this does not hold for all the years. Contributions from the Bering Sea (BeS) winds is highly variable in sign. Due to competition with other regions, it does not alone determine the sign of the annual-mean anomaly. Overall, the upstream contributions to Bering Strait transport originating from the Northwest Pacific (Pa) and Gulf of Alaska (GoA) are small (∼3%) except for the years 2005 and 2011 where they are large enough to offset the contribution from the Bering Sea and result in a change of sign of the annual mean transport anomaly in the model.

In the two extreme years, 2004 and 2012, contributions from the combined La and Ba are more prominent. Annual transports for these two years, in addition to 2007, are

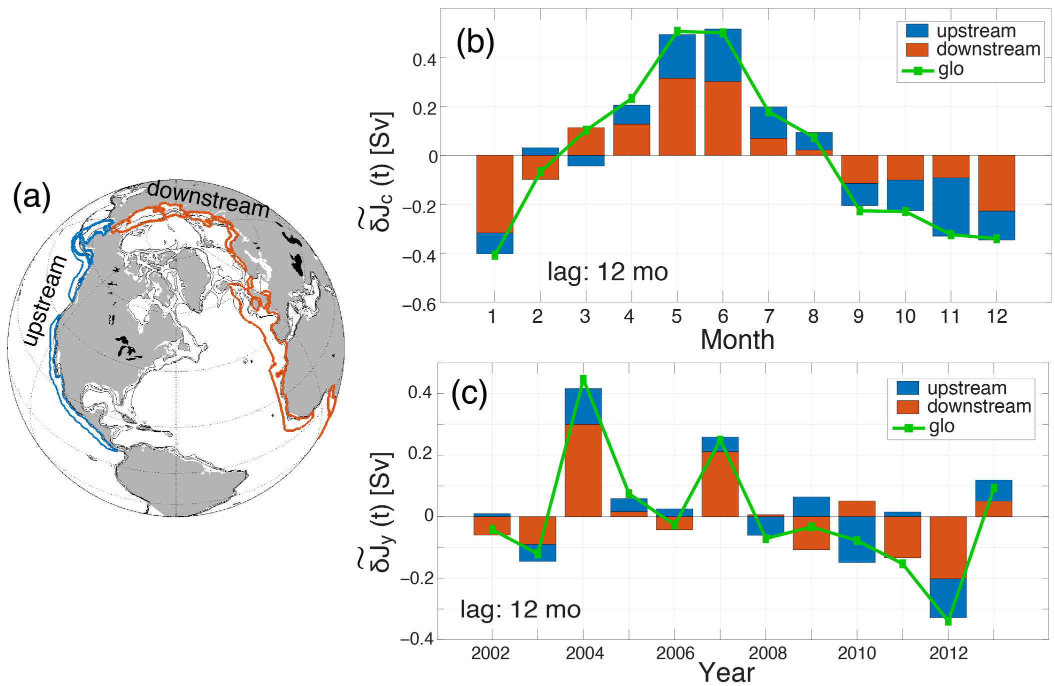

Figure 7. Same as Fig. 6, but partitioned in terms of contributions up-stream (south) and down-stream (north) of the Bering Strait, relative to the mean flow, which is northward through the strait.

the primary factors determining the decline in the model annual transports between 2002–2013, and may have some bearing on the difference between the model and observed trends.

The relationship between the extreme years and the regional contribution give insight into the debate as to whether the Bering Strait throughflow is forced from the Pacific in the direction of the mean flow through the strait which is northward) or the Arctic/Atlantic (downstream). The traditional view of the dominance of Pacific origin forcing has been recently challenged Peralta-Ferriz and Woodgate (2017). Fig. 7 splits the contributions shown in Fig. 6 into only up- and down-stream components. Seasonally (Fig. 7b), the results support the conclusions of Peralta-Ferriz and Woodgate (2017), that the summer transports variability are more strongly related to perturbations over the Arctic (downstream), although the upstream Pacific-forced component is still significant. In the fall, forcing over the Pacific is more important, although forcing over the Arctic still plays a significant role. Interannually (Fig. 7c), both Pacific and Arctic/Atlantic forcings provide significant contributions. Where their influences are coherent, maxima/minima in transports are typically found (2004, 2007, 2012). However, the downstream Arctic/Atlantic contributions are generally larger and more highly correlated with the total annual anomaly (correlation coefficient $\rho(\widetilde{\delta J_{downstream}}, \delta J_{fwd}) = 0.94$ compared to $\rho(\widetilde{\delta J_{upstream}}, \delta J_{fwd}) = 0.74$), and can usually predict the sign of the total anomaly (with the exception being the year 2010).

We can go one step further and inspect the individual forcing anomalies in the eight regions highlighted in Fig 6 to identify if any particular distribution of regional forcing anomalies determine the three years of the transport extrema (2004, 2007, and 2012). One strong correlation (correlation coefficient of 0.84) can be identified, as shown in Fig. 8, between the combined $\delta\tau_E$ for the combined downstream regions Ck+ESS+La+Ba (grey) and the annual BE transports anomalies δJ (black line).

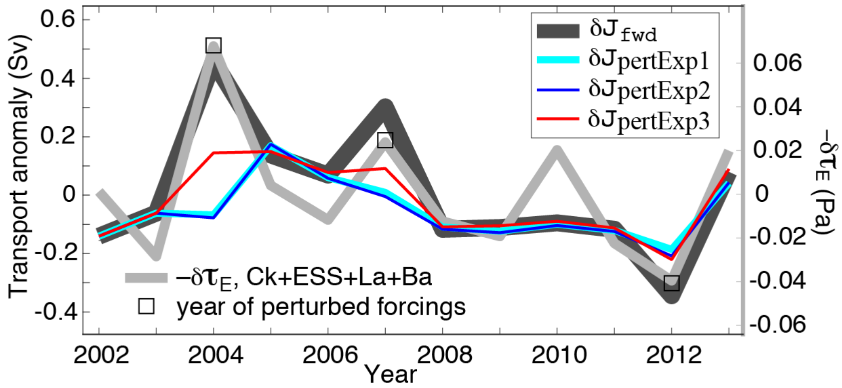

Figure 8. Minus eastward wind stress anomalies (light-gray, right y-axis) and transport anomalies (left y-axis) for the forward run (δJ_{fwd}, thick dark gray) and perturbation experiments pertExp1–3 as per key. Black squares mark 2004, 2007, and 2012, the years when the extrema of the Eastward wind stress anomalies coincide with those of forward transport anomalies. In the perturbation runs, for these three years (2004, 2007, 2012), the surface forcings were replaced with the prior years as detailed in Table. 1.

Table 1. List of perturbation experiments which modify the atmospheric forcing for the three years (2004, 2007, and 2012) when extrema of Eastward wind stresses anomalies $\delta\tau_E$ within the regions Ck+ESS+La+Ba coincides with extrema of Bering Strait northward volume transports $\widetilde{\delta J}$. For these three years, the original surface forcing fields (second column) are replaced with the forcings from the previous years as listed in the third column. The geographic extent over which these atmospheric fields were perturbed is indicated in the fourth column.

Experiment	Original surface forcing fields	Replaced surface forcing fields	Perturbed regions
pertExp1	$\text{all}_{\{2004,2007,2012\}}$	$\text{all}_{\{2003,2006,2011\}}$	global
pertExp2	$\tau_{[N,E],\{2004,2007,2012\}}$	$\tau_{[N,E],\{2003,2006,2011\}}$	global
pertExp3	$\tau_{[N,E],\{2004,2007,2012\}}$	$\tau_{[N,E],\{2003,2006,2011\}}$	within ∼10 km and including regions Ck+ESS+La+Ba

Given the corresponding peaks (positive and negative) of $\delta\tau_E$ and δJ, we can deduce that large τ_E anomalies in these regions downstream of the Bering Strait (Ck+ESS +La+Ba) are responsible for the extrema in the model δJ. To confirm this, we performed a series of perturbation experiments as listed in Table. 1. In the first experiment, pertExp1, all global surface forcing fields for the three years 2004, 2007, and 2012 are replaced by the corresponding prior years (2003, 2006, 2011). In the second experiment, pertExp2, only the surface wind stresses are replaced. pertExp3 is the same as pertExp2, except that only wind stresses within ∼10 km of the regions Ck+ESS+La+Ba are perturbed (see Table. 1).

Based on the geographic distribution of the adjoint sensitivity and reconstruction up to this point (Fig. 6), we expect pertExp1 and pertExp2 to yield nearly identical results due to the negligible contributions of other forcing fields besides wind stresses on the Bering Strait northward transports. We also anticipate that the transport extrema in 2004, 2007, and 2012 would be significantly reduced and approach those of the previous years (provided that competitions from other regions not identified in Fig. 8 are not dominant). This is indeed confirmed in the results summarized in Fig. 8 (blue, green, and red curves). Specifically, $\delta J_{pertExp[1,2]}$ are practically identical. Transport anomalies for the years 2004, 2007, 2012 are significantly reduced and are close to the δJ in the years of the same forcing. A similar experiment (not shown) indicates that using the forcing from extreme years (2004, 2007, 2012) on other years yields almost equally extreme transports.

Lastly, in pertExp3 (red curve in Fig. 8), we test to what extent this result is driven by wind perturbation only in the identified regions of interest, by changing the wind stress fields only within regions Ck+ESS+La+Ba and a buffer zone of order ∼10 km outside. Results indicate that changing τ_E only within the regions Ck+ESS+La+Ba identified in Fig. 6 is all by itself sufficient to significantly reduce the transport extrema magnitudes, although not as much as those with the original forcings. While one might test how sensitive the size of the buffer zone is to the transport extrema magnitudes, we feel such experiments are unjustified at present since wind stresses over the Arctic Ocean are known to have large uncertainties due to lack of observations (Chaudhuri et al., 2014; Liu et al., 2015). Note also that this final experiment, by imposing a wind stress anomaly in a restricted region, creates an atmospheric forcing field which is no longer self consistent, and thus results must be taken with some caution. Our results do indicate, nevertheless, that wind stress anomalies in several key regions are primary controlling factors in determining the transport results in the model. The result also underlines the importance of improving the accuracy of wind stresses in atmospheric reanalyses.

4 Discussion

4.1 Regions of Influence

Our work suggests the dominant forcing of the Bering Strait transport anomalies to be local and with only little time lag, but there are also remote, longer timescale influences, as shown by Fig. 6. Continental shelf waves and coastally trapped Kelvin waves have been suggested as important mechanisms for transferring perturbations along coasts in general, (e.g., Brink (1991), Heimbach et al. (2011)) and in the context of influencing the Bering Strait throughflow in particular (Danielson et al., 2014). The sensitivity patterns are consistent with propagation directions of such waves in the northern hemisphere (i.e., with the coast to their right), with the important regions of influence all located upstream in the Kevin/shelf wave-propagation sense of the strait. Fig. 9 shows the sensitivities of δJ to wind stress, now highlighting the directions of Kelvin/shelf wave propagation that can contribute to positive δJ. For each subplot, the sensitivity is normalized by its maximum magnitude at each corresponding lag to highlight the spatial distribution and time-scale of propagation along the coastal regions. We ask next if the timescales are reasonable.

Previous observational studies of multi-decadal sea surface height records along the Siberian and Laptev Sea Shelves showed presence of shelf waves with velocity 1.3–5.2 m/s and periods of less than 60 days (Voinov & Zakharchuk, 1999) associated with wind perturbations parallel and perpendicular to the coast. Further upstream in the Barents Sea and along the Norwegian coast, numerical and theoretical calculations by Drivdal et al. (2016) support evidence of the presence of coastal Kelvin waves and continental shelf waves generated by atmospheric storms with a phase speed of 5–24 m/s and a period ∼44 hours. Estimating the length of the east Siberian and Laptev Sea Shelves as ∼4600 km yields a timescale of about 10–40 days for coastal shelf waves originated from these shelves to reach Bering Strait, a time-frame consistent with Fig. 9a–b. Similarly, the additional distance to traverse along the coast in the Barents and Nordic Seas of 8000 km at wave speeds

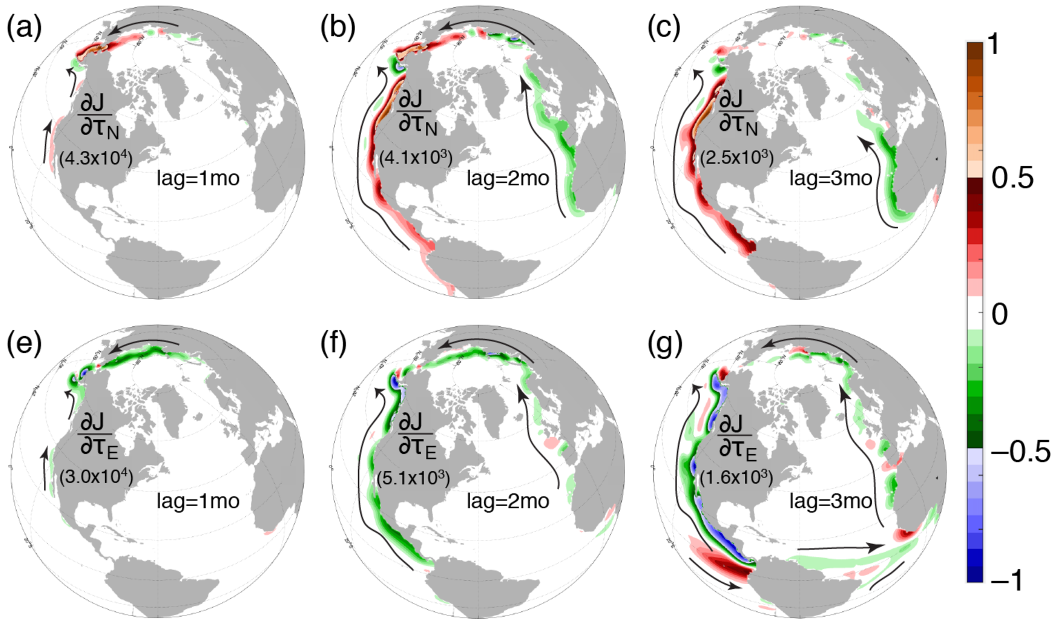

Figure 9. Normalized sensitivity (factor given on each plot) to τ_N (a-c) and τ_E (e-g) for lags of 1–3 months (columns). Arrows indicate direction of propagation of Kelvin and shelf waves. Geographical influence in time (reaching from the Pacific/Atlantic oceans in 2 months, and from the equator at 3 months lags) are consistent with wave speed estimates as discussed in the text. Note that scale factor varies by a factor of $\sim$20 across the different lags.

5–24 m/s yields an additional 4–20 days, which is also consistent with the two-month lag of waves originating along these coastal regions to reach the Bering Strait.

Within three months, sensitivities can be traced to the equatorial Kelvin wave-guide paths (wave speed $\sim$1–3 m/s, (Eriksen et al., 1983) over a distance $\sim$7300 km, yielding a transit time of 28–84 days) in both the Pacific and Atlantic Oceans (Heimbach et al., 2011). As information is more dispersed spatially, the magnitude of sensitivities decreases such that the total contributions of all regions to wind perturbations at this lag only contribute $\sim$1% to the total BE transport. Note that the high or low sensitivity by itself does not solely determine the magnitude of the contribution to transport δJ from that region, since the final contribution to transport depends on the sum through various lags of the product of sensitivity and the forcing anomaly.

In terms of wind stress magnitude and direction, as indicated by the color scale in Fig. 9, northwestward wind stress (positive τ_N, negative τ_E) along the coast in the Pacific contribute primarily to positive increase in $\widetilde{\delta J}$ at Bering Strait. Similarly, along the coast of the East Siberian and Laptev Seas, northwestward wind stress gives positive $\widetilde{\delta J}$. Further upstream along the coast in the Barents and Nordic Seas and in the eastern margin of the Atlantic Ocean, southwestward wind stress contribute to positive $\widetilde{\delta J}$. This is consistent results from Peralta-Ferriz and Woodgate (2017) which shows that winds that invoke onshore (offshore) Ekman flow in the Bering+Pacific sector (Arctic + Barents + Nordic + Atlantic sector) are related to positive flow anomalies at the strait.

4.2 The Effect of Precipitation

The majority of work in this paper has focused on the impacts of wind stress anomalies on the flow variations through the strait, as that was found to be the greatest driver

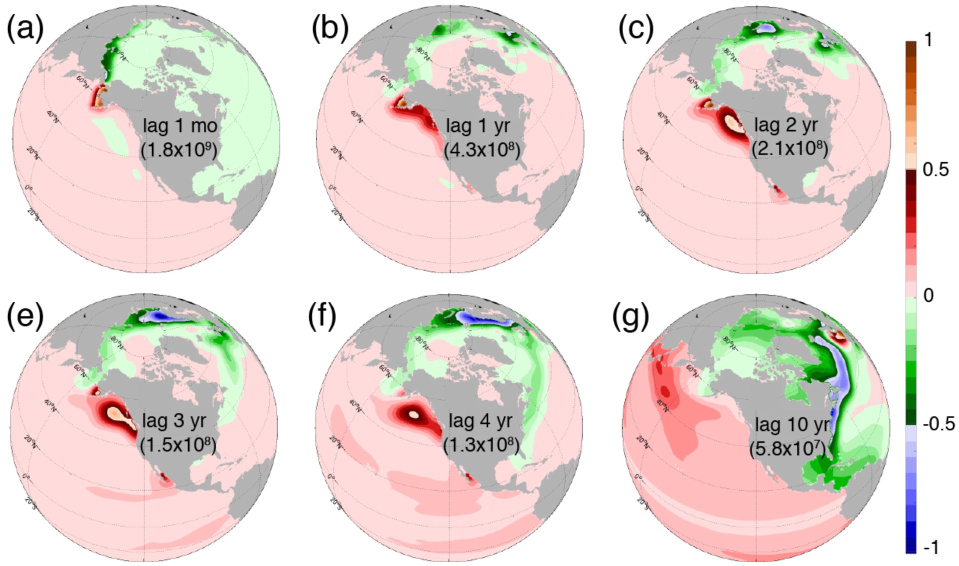

Figure 10. (a) Normalized adjoint sensitivity to precipitation (positive precipitation implies adding freshwater to the ocean) for time lags from 1 month to 10 years. The normalization factor is the maximum magnitude of sensitivity at each lag and is given on each plot. Note that the normalization factor varies by a factor of ∼30 across the plots.

in the adjoint experiments performed. The method, however, allows us to examine the impact of other forcings as well – e.g., precipitation which is also hypothesized to be a driver of the Bering Strait flow (Stigebrandt, 1984)).

Fig. 10 shows the sensitivity of the BE transport anomaly to precipitation perturbations for lags ranging from 1 month to 10 years. Summing these show the total contribution to Bering Strait flow variability to be small (order of 0.01Sv). However, the patterns are themselves interesting. At 1 month lag, BE flow is enhanced by positive net precipitation over the Bering Sea Shelf and negative net precipitation over the east Siberian Sea. This pattern enhances the steric sea surface slope through the strait, mechanistically increasing northward flow, as per the steric driving of the flow due to the global freshwater cycle as suggested by Stigebrandt (1984). At longer lags of 1–4 years, the region of sensitivity to positive precipitation is further south (along the Alaskan Coast) while the region where negative precipitation enhances the flow now extends further along the Russian coast and into the Bering Sea. Note that these lags are much larger than the few-month lags for wind stress forcings, indicative of the difference between the wave speeds of a few m/s and advective speeds of waters of order of a few cm/s.

Precipitation influences emerge along the Gulf Stream paths in the North Atlantic after 3 years (Fig. 10e-g) and along the Kuroshio path in the North Pacific after 4 years (Fig. 10f-g) . In general, the sign of the sensitivity is consistent with the steric "pressure head" hypothesis (Stigebrandt, 1984) that negative (positive) $\delta precip$ into the Atlantic (Pacific) Ocean would increase the steric sea surface height difference between the two oceans and promote increased in δJ at the strait. However, given that the magnitude of $\partial J/\partial precip$ of O∼ (10^9) $m^3/s/m/s$ and that $\delta precip$ is of the order O∼ $(10^{-8} m/s$, δJ_{precip} is of the order O∼ (10^1) m^3/s or $(10^{-5} Sv$ which is significantly smaller than contributions from wind stress, we conclude that these patterns, though interesting, are not of much relevance, and advective/wind-driven effects are a much larger forcing of the Bering Strait throughflow than the steric term, at least on timescales of months to years, as De Boer and Nof (2004b) and De Boer and Nof (2004a) have suggested. Note that since we are considering anomalies, we cannot draw direct conclusions about the forcing of the **mean** of the Bering Strait transport, which may still have a significant steric term.

5 Conclusions

The goal of our study is to understand the mechanisms controlling the transport variability of the Bering Strait throughflow. To this end, we use a modeling tool to understand causes of variability in a global sea ice-ocean general circulation model. If controlling mechanisms can be systematically understood from the model, we enhance our ability to identify dynamical forcing terms that can contribute to the volume transport variability at the strait. Here, the adjoint modeling framework of the 1° ECCO version 4 global configuration, which has been shown to be an effective tool to investigate ocean-sea ice dynamical processes, is used to investigate the possible mechanisms controlling the variability of the Bering Strait volume transport.

The sensitivities of the volume transport anomalies (compared to a 2002-2013 mean) to atmospheric forcing perturbations are used to reconstruct the Bering Strait (BE) transport variability (Fig. 2). The time-series of the transport anomaly can be reconstructed, eqn. (3), with high fidelity, with correlation coefficients ranging from 0.94–0.98 and percentage of explained variance (PEV) of 88–97% (Fig. 4) when compared to the forward model transport anomalies, quantified using the full model dynamics. These results suggest that the response is sufficiently linear for the adjoint model to be used to deduce causal mechanisms for the transport variability.

The adjoint sensitivities show that the model's Bering Strait transport anomaly is controlled primarily by the wind stress on short time-scales of order 1–5 months, with the percentage of explained monthly variance of the flow being $\sim$90% and 92% within the first month and the first five months, respective (Fig. 3). Other atmospheric forcing terms (precipitation, radiative fluxes, water vapor content, air temperature) have negligible ($<$ 1%) influence on both short (monthly) and long-term (decadal) variability (Fig. 3, 4).

The model's transport variability at various temporal scales can be reconstructed to high fidelity by convolving adjoint sensitivities with wind stress forcing, with correlations between the reconstructed and the forward model BE transport anomalies of $\sim$95%, 99%, and 98% at monthly, seasonal, and interannual time-scales, respectively (Fig. 4). Spatial decomposition indicates that on short time-scales (monthly) winds over the Bering Shelf and the combined Chukchi and East Siberian regions are the most significant drivers, and each region contributes approximately equal amounts in magnitudes to the net transport anomalies ($\sim$ 40% each, Fig. 5), with the combined Chukchi and East Siberian regions being slightly more influential. This is consistent with recent results from Peralta-Ferriz and Woodgate (2017), who found the East Siberian Sea to be more dominant in controlling the transport than the Bering Sea, especially in summer, although in winter the Bering Shelf had a greater influence. Sensitivity patterns indicative of coastally trapped adjoint wave propagation (Fig. 6, 9, 10) lead us to hypothesize that continental shelf waves and coastally-trapped waves are the dominant mechanisms for propagating information from up-stream in the Kelvin wave sense) to the strait. Further support for this hypothesis comes from a reasonable match of timescales of propagation of influences with wave speed estimates from the literature and findings from prior work by Danielson et al. (2014).

Including wind-stress influence from regions further away from the strait in the reconstruction yields a similar conclusion that the Bering Sea Shelf, the Chukchi Sea, and the East Siberian Sea remain the dominant drivers of the Bering Strait flow variability (80% combined), with additional contribution of influences from the Barents and Nordic

Seas, the eastern Pacific Ocean and eastern Atlantic Ocean (Fig. 6). These far field influences contribute ∼20% of the monthly-scale variability (Fig. 5b) and ∼30% of the seasonal variability (Fig. 6b).

To address the long standing question as to whether the flow variability is driven from the Pacific or the Arctic/Atlantic sector, we compare the influences of forcing anomalies from these two regions (Fig. 7). We conclude that both upstream and downstream regions are important, and that when their influences act in concert, the result is usually a year of extreme high or low transport. Interestingly, the downstream Arctic/Atlantic forcings are better at predicting anomalous flow than the upstream (correlation coefficient $\rho(\widetilde{\delta J}_{downstream}, \delta J_{fw}) = 0.94$ compare to $\rho(\widetilde{\delta J}_{upstream}, \delta J_{fw}) = 0.74$)). An important conclusion is the recognition that the Arctic shelves play a substantial role in determining the Bering Strait flow variability.

In most years, no clear correlation can be established between the regional contributions and the overall year-to-year annual-mean anomaly (Fig. 6). Nevertheless, for the three years with transport extrema, 2004, 2007 and 2012, eastward wind stress anomalies in the combined Chukchi, East Siberian, Laptev, and Barents Seas regions are found to be the main driving force (Fig. 8). Perturbation experiments showed the extreme transports to be closely linked to the wind stress forcing of that year, with a large amount of the effect being strongly tied to the local wind stress in these key regions (Table. 1, Fig. 8).

Previous studies have suggested steric effects to drive the flow (e.g., Stigebrandt (1984); Aagaard et al. (2006)). Our results, based on patterns of sensitivity to precipitation are consistent in sign with the existing hypothesis that the BE transport is sensitive to the steric sea surface height difference between the Atlantic and Pacific oceans (Fig. 10), our study shows the resultant contribution to the transport variability is small ($< 1\%$). It should be noted that, since we are only able to consider the driving forces of transport *anomalies*, we cannot describe what might be driving the mean flow. Our results here support previous findings (De Boer & Nof, 2004b, 2004a) of the importance of basin-scale winds Peralta-Ferriz and Woodgate (2017), in driving the Bering Strait transport variability.

In contrast to previous work, which is based on simple theoretical or statistical models, our results are based on the use of the dynamically and kinematically consistent state-estimation framework and the detailed analysis of adjoint model-derived sensitivities to conduct dynamical attributions. These results yield more physical insights than is usually obtained from purely statistical methods. Our findings of the impact of local and far field forcings on the flow are a substantial advance in our understanding of the mechanisms driving transport variability at the Bering Strait. Another key finding is the importance of the Arctic (especially the Chukchi and the East Siberian and Laptev Seas) on the flow variability, contrasting the prior assumptions that the flow is driven primarily from the south. Lastly, the short-term and localized response of the strait transport anomalies to the forcing suggests also some predictive skill if sufficiently accurate wind stress fields, especially in the Arctic, are available.

Acknowledgments

This work was supported by NSF OPP grants 1304050 and 1603903, and by NSF Arctic Observing Network grants PLR-1304052 and PLR 1758565. Additional support for PH came from a JPL/Caltech subcontract for the "Estimating the Circulation and Climate of the Ocean" project. The Bering Strait mooring data are freely available via the Bering Strait Observing Network website (psc.apl.washington.edu/BeringStrait.html) and the permanent US oceanographic data archives at the National Centers for Environmental Information (www.nodc.noaa.gov).

References

Aagaard, K., Weingartner, T. J., Danielson, S. L., Woodgate, R. A., Johnson, G. C., & Whitledge, T. E. (2006). Some controls on flow and salinity in Bering strait. *Geophys. Res. Lett.*, *33*(19). doi: 10:1029/2006GL026612

Arrigo, K. R. (2014). Sea ice ecosystems. *Annual Review of Marine Science*, *6*(1), 439-467. (PMID: 24015900) doi: 10.1146/annurev-marine-010213-135103

Arrigo, K. R., Perovich, D. K., Pickart, R. S., Brown, Z. W., van Dijken, G. L., Lowry, K. E., ... Swift, J. H. (2012). Massive Phytoplankton Blooms Under Arctic Sea Ice. *Science*. doi: 10.1126/science.1215065

Brink, K. (1991). Coastal-trapped waves and wind-driven currents over the continental shelf. *Annu. Rev. Fluid Mech.*, *23*, 389–412.

Chaudhuri, A., Ponte, R., Forget, G., & Heimbach, P. (2013). A comparison of atmospheric reanalysis surface products over the ocean and implications for uncertainties in air-sea boundary forcing. *J. Climate*, *26*, 153–170. doi: JCLI-D-12-00090.1

Chaudhuri, A., Ponte, R., & Nguyen, A. (2014). A comparison of atmospheric reanalysis products for the Arctic Ocean and implications for uncertainties in air-sea fluxes. *J. Climate*, *27*(14), 5411–5421. doi: http://dx.doi.org/10.1175/JCLI-D-13-00424.1

Coachman, L., & Aagaard, K. (1966). On the water exchange through Bering strait. *Limonology and Oceanogr.*, *11*(1), 44–59. doi: 10:4319/lo.1966.11.1.0044

Danielson, S. L., Weingartner, T. J., Hedstrom, K. S., Aagaard, K., Woodgate, R. A., Chuchitser, E., & p.J. Stabeno. (2014). Coupled wind-forced controls of the Bering-Chukchi shelf circulation and the Bering strait throughflow: Ekman transport, continental shelf waves, and variations of the Pacific-Arctic sea surface height gradient. *Progress in Oceanogr.*, *125*, 40–61. doi: http://dx.doi.org/10.1016/j.pocean.2014.04.006

De Boer, A., & Nof, D. (2004a). The Bering Strait's grip on the northern hemisphere climate. *Deep-Sea Res., Part I*, *51*(10), 1347–1366. doi: 10.1016/j.dsr.2004.05.003

De Boer, A., & Nof, D. (2004b). The exhaust valve of the North Atlantic. *J. Climate*, *17*(3), 417–422. doi: 10.1175/1520-0442

Dee, D. P., Uppala, S. M., Simmons, A. J., Berrisford, P., Poli, P., Kobayashi, S., ... Vitart, F. (2011). The ERA-Interim reanalysis: configuration and performance of the data assimilation system. *Q. J. R. Meteorol. Soc.*, *137*(656), 553–597. doi: 10.1002/qj.828

Drivdal, M., Weber, J., & Debernard, J. (2016). Dispersion relation for continental shelf waves when the shallow shelf part has an arbitrary width: Application to the shelf west of Norway. *Journal of Physical Oceanography*, *46*(2), 537-549. doi: 10.1175/JPO-D-15-0023.1

Eriksen, C., Blumenthal, M., Hayes, S., & Ripa, P. (1983). Wind-generated equatorial Kelvin waves observed across the Pacific Ocean. *Journal of Physical Oceanography*, *13*, 1622–1640.

Fenty, I., & Heimbach, P. (2013). Coupled sea ice-ocean state estimation in the Labrador Sea and Baffin Bay. *J. Phys. Ocean.*, *43*(6), 884–904. doi: 10.1175/

JPO-D-12-065.1

Fenty, I., Menemenlis, D., & Zhang, H. (2015). Global coupled sea ice-ocean state estimate. *Clim. Dyn.*. doi: 10.1007/s00382-015-2796-6

Forget, G., Campin, J. M., Heimbach, P., Hill, C. N., Ponte, R. M., & Wunsch, C. (2015). ECCO version 4: an integrated framework for non-linear inverse modeling and global ocean state estimation. *Geosci. Model Dev.*, *8*, 3071-3104. doi: 10.5194/gmd-8-3071-2015

Fukumori, I., Heimbach, P., Ponte, R. M., & Wunsch, C. (2018). A dynamically consistent, multi-variable ocean climatology. *Bulletin of the American Meteorological Society*, null. doi: 10.1175/BAMS-D-17-0213.1

Fukumori, I., Wang, O., Llovel, W., Fenty, I., & Forget, G. (2015). A near-uniform fluctuation of ocean bottom pressure and sea level across the deep ocean basins of the Arctic Ocean and the Nordic Seas. *Progress in Oceanography*, *134*(C), 152–172.

Heimbach, P., Fukumori, I., Hill, C. N., Ponte, R. M., Stammer, D., Wunsch, C., ... Zhang, H. (2019). Putting It All Together: Adding Value to the Global Ocean and Climate Observing Systems With Complete Self-Consistent Ocean State and Parameter Estimates. *Frontiers in Marine Science*, *6*, 769–10.

Heimbach, P., Menemenlis, D., Losch, M., Campin, J., & Hill, C. (2010). On the formulation of sea-ice models. part 2: Lessons from multi-year adjoint sea-ice export sensitivities through the Canadian Arctic Archipelago. *Ocean Modeling*, *33(1-2)*, 145-158. doi: 10.1016/j.ocemod.2010.02.002

Heimbach, P., Wunsch, C., Ponte, R. M., Forget, G., Hill, C., & Utke, J. (2011). Timescales and regions of the sensitivity of Atlantic meridional volume and heat transport: Toward observing system design. *Deep Sea Research Part II: Topical Studies in Oceanography*, *58*(17-18), 1858–1879. doi: 10.1016/j.dsr2.2010.10.065

Hu, A., & Meehl, G. (2005). Bering Strait throughflow and the thermohaline circulation. *Geophys. Res. Lett.*, *32*(L24610). doi: 10.1029/2005GL024424

Hu, A., Meehl, G., Han, W., Timmermann, A., Otto-Bliesner, B., Liu, Z., ... Wu, B. (2012). Role of the Bering Strait on the hysteresis of the ocean conveyor belt circulation and glacial climate stability. *Proceedings of the National Academy of Sciences of the United States of America*, *109*(17), 6417–6422. doi: 10.1073/pnas.1116014109

Jakobsson, M., Mayer, L. A., Coakley, B., Dowdeswell, J. A., Forbes, S., Fridman, B., ... Weatherall, P. (2012). The International Bathymetric Chart of the Arctic Ocean (IBCAO) Version 3.0. *Geophysical Research Letters*. doi: 10.1029/2012GL052219

Kalnay, E., Kanamitsu, M., Kistler, R., Collins, W., Deaven, D., Gandin, L., ... Reynolds, R. (1996). The NCEP/NCAR 40-Year Reanalysis Project. *Bulletin of the American Meteorological Society*, *77*(3), 437-471. doi: 10.1175/1520-0477(1996)077⟨0437:TNYRP⟩2.0.CO;2

Kobayashi, S., Ota, Y., Harada, Y., Ebita, A., Moriya, M., Onoda, H., ... Takahashi, K. (2015). The JRA-55 Reanalysis: General Specifications and Basic Characteristics. *Journal of the Meteorological Society of Japan*, *93*(1), 5–48.

Lammers, R. B., & Shiklomanov, A. I. (2001). Assessment of contemporary Arctic river runoff based on observational discharge records. *J. Geophys. Res.*, *106*(D4), 3321.

Liu, Z., Schweiger, A., & Lindsay, R. (2015). Observations and modeling of atmospheric profiles in the Arctic seasonal ice zone. *Monthly Weather Review*, *143*(1), 39-53. doi: 10.1175/MWR-D-14-00118.1

Onogi, K., Tsutsui, J., Koide, H., Sakamoto, M., Kobayashi, S., Hatsushika, H., ... Taira, R. (2007). The JRA-25 Reanalysis. *J. Meteor. Soc. Japan*, *85*(3), 369–432.

Peralta-Ferriz, A. C., & Woodgate, R. A. (2017). The dominant role of the East

Siberian Sea in driving the oceanic flow through the Bering Strait - Conclusions from GRACE ocean mass satellite data and in situ mooring observations between 2002 and 2016. *Geophysical Research Letters*, *44*, 11,472–11,481. doi: 10.1002/2017GL075179

Pillar, H., Heimbach, P., Johnson, H., & Marshall, D. (2016). Dynamical attribution of recent variability in Atlantic overturning. *J. Clim.*, *29*, 3339–3352. doi: 10.1175/JCLI-D-15-0727.1

Serreze, M. C., Barrett, A. P., Slater, A. G., Steele, M., Zhang, J., & Trenberth, K. E. (2007). The large-scale energy budget of the Arctic. *J. Geophys. Res.*, *112*(C11122). doi: 10.1029/2006JD008230

Serreze, M. C., Barrett, A. P., Slater, A. G., Woodgate, R. A., Aagaard, K., Lammers, R. B., ... Lee, C. M. (2006). The large-scale freshwater cycle of the Arctic. *J. Geophys. Res.*, *111*(C11010). doi: 10.1029/2005JC003424

Serreze, M. C., Crawford, A. D., Stroeve, J., Barrett, A. P., & Woodgate, R. A. (2016). Variability, trends, and predictability of seasonal sea ice retreat and advance in the Chukchi Sea. *J. of Geophys. Res.*. doi: 10.1002/2016jc011977

Shiklomanov, A. I., Yakovleva, T. I., Lammers, R. B., Karasev, I. P., Vörösmarty, C. J., & Linder, E. (2006). Cold region river discharge uncertainty—estimates from large Russian rivers. *Journal of Hydrology*, *326*(1-4), 231–256.

Smith, T., & Heimbach, P. (2018). Atmospheric origins of variability in the South Atlantic meridional overturning circulation. *Journal of Climate*, *32*, 1483–1500. doi: https://doi.org/10.1175/JCLI-D-18-0311.1

Stammer, D. (2005). Adjusting Internal Model Errors through Ocean State Estimation. *J. Phys. Oceanogr.*, *35*(6), 1143–1153.

Stammer, D., Balmaseda, M., Heimbach, P., Köhl, A., & Weaver, A. (2016). Ocean data assimilation in support of climate applications: Status and perspectives. *Annu. Rev. Mar. Sci.*, *8*(accepted). doi: 10.1146/annurev-marine-122414-034113

Stigebrandt, A. (1984). The North Pacific: a global-scale estuary. *J. Phys. Oceanogr.*, *14*(2), 464–470.

Toulany, B., & Garrett, C. (1984). Geostrophic control of fluctuating barotropic flow through straits. *Journal of Physical Oceanography*, *14*(4), 649-655. doi: 10.1175/1520-0485(1984)014⟨0649:GCOFBF⟩2.0.CO;2

Uppala, S. M., KAllberg, P. W., Simmons, A. J., Andrae, U., Bechtold, V. D. C., Fiorino, M., ... Woollen, J. (2005). The era-40 re-analysis. *Quarterly Journal of the Royal Meteorological Society*, *131*(612), 2961–3012. doi: 10.1256/qj.04.176

Voinov, G., & Zakharchuk, E. (1999). Large-Scale Variations of Sea Level in the Laptev Sea. In H. Kassens et al. (Eds.), (pp. 25–36). Berlin, Heidelberg: Springer Berlin Heidelberg.

Wadley, M. R., & Bigg, G. R. (2002). Impact of flow through the Canadian Archipelago and Bering Strait on the North Atlantic and Arctic circulation: An ocean modelling study. *Quarterly Journal of the Royal Meteorological Society*, *128*(585), 2187–2203. Retrieved from `http://dx.doi.org/10.1256/qj.00.35` doi: 10.1256/qj.00.35

Walsh, J., Dieterle, D., Muller-Karger, F., Aagaard, K., Roach, A., Whitledge, T., & Stockwell, D. (1997). CO2 cycling in the coastal ocean. II. Seasonal organic loading of the Arctic Ocean from source waters in the Bering Sea. *Continental Shelf Research*, *17*(1), 1–36.

Weingartner, T., Danielson, S., & Royer, T. (2005). Freshwater variability and predictability in the Alaska Coastal Current. *Deep Sea Research II*, *52*, 169–191.

Woodgate, R. A. (2018). Increases in the Pacific inflow to the Arctic from 1990 to 2015, and insights into seasonal trends and driving mechanisms from year-round Bering Strait mooring data. *Progress in Oceanography*, *160*, 124–154. doi: https://doi.org/10.1016/j.pocean.2017.12.007

Woodgate, R. A., Aagaard, K., & Weingartner, T. J. (2005a). Monthly temperature, salinity, and transport variability of the Bering Strait through flow. *Geophys. Res. Lett.*, *32*(L04601). doi: 10.1029/2004GL021880

Woodgate, R. A., Aagaard, K., & Weingartner, T. J. (2005b). A year in the physical oceanography of the Chukchi Sea: Moored measurements from autumn 1990-1991. *Deep-Sea Res., Part II*, *52*(24–26), 3116–3149. doi: 10.1016/j.dsr2.2005.10.016

Woodgate, R. A., Aagaard, K., & Weingartner, T. J. (2006). Interannual changes in the bering strait fluxes of volume, heat and freshwater between 1991 and 2004. *Geophys. Res. Lett.*, *33*(L15609), 10.1029/2006GL026931.

Woodgate, R. A., Stafford, K. J., & Prahl, F. G. (2015). A synthesis of year-round interdisciplinary mooring measurements in the Bering Strait (1990–2014) and the RUSALCA years (2004–2011). *Oceanography*, *28*(3), 46–67. doi: 10.5670/oceanog.2015.57

Woodgate, R. A., Weingartner, T., & Lindsay, R. (2010). The 2007 Bering Strait oceanic heat flux and anomalous Arctic sea-ice retreat. *Geophys. Res. Lett.*, *37*(L01602). doi: 10.1029/2009GL041621

Woodgate, R. A., Weingartner, T., & Lindsay, R. (2012). Observed increases in Bering Strait oceanic fluxes from the Pacific to the Arctic from 2001 to 2011 and their impacts on the Arctic Ocean water column. *Geophys. Res. Lett.*, *39*(L24603). doi: 10.1029/2012GL054092

Wunsch, C., & Heimbach, P. (2007). Practical global oceanic state estimation. *Physica D: Nonlinear Phenomena*, *230*(1-2), 197–208. doi: 10.1016/j.physd.2006.09.040

Wunsch, C., & Heimbach, P. (2013). Dynamically and Kinematically Consistent Global Ocean Circulation and Ice State Estimates. In *Ocean circulation and climate: A 21st century perspective* (pp. 553–579). Elsevier Ltd. doi: 10.1016/B978-0-12-391851-2.00021-0